



Design of highly stable MgO promoted Cu/ZnO catalyst for clean methanol production through selective hydrogenation of CO₂

Sachin Kumar Sharma^{a,b}, Tuhin Suvra Khan^{a,b}, Rajib Kumar Singha^a, Bappi Paul^{a,c}, Mukesh Kumar Poddar^a, Takehiko Sasaki^d, Ankur Bordoloi^a, Chanchal Samanta^e, Shelaka Gupta^f, Rajaram Bal^{a,b,*}

^a Light Stock Processing Division, CSIR-Indian Institute of Petroleum, Dehradun, 248005, India

^b Academy of Scientific and Innovative Research (AcSIR), Ghaziabad, 201002, India

^c Department of Chemistry, National Institute of Technology Nagaland, Dimapur, Nagaland, 797103, India

^d Department of Complexity Science and Engineering, Graduate School of Frontier Science, The University of Tokyo, Kashiwanoha, Kashiwa-shi, Chiba, 277-8561, Japan

^e Bharat Petroleum Corporation Ltd., Greater Noida, Uttar Pradesh, 201306, India

^f Department of Chemical Engineering, Indian Institute of Technology Hyderabad, Kandi, 502285, Sangareddy, Telangana, India

ARTICLE INFO

Keywords:

Cu-Nanoparticles
MgO promotor
CO₂ hydrogenation
Methanol
DFT-study

ABSTRACT

The synergistic interaction between small Cu particles and MgO/ZnO-supported catalysts, synthesized by the hydrothermal method, show a very high methanol production rate ($0.0063 \text{ mol g}_{\text{Cu}}^{-1} \text{ h}^{-1}$). High Cu dispersion and large Cu surface area in the hydrothermal synthesized Cu/MgO/ZnO catalyst postulated to be the reason for high activity. The formation of defected ZnO crystals with Mg atoms provided a better adsorption site for CO₂ (near Mg atom), whereas Cu-ZnO interface sites are responsible for the activation of CO₂. 20 wt% loaded MgO catalyst showed preference to selective CO₂ hydrogenation pathway producing clean methanol with > 99 % selectivity. In addition, Density Functional Theory (DFT) studies revealed that the basic nature of the MgO support can be the probable reason for the higher CO₂ adsorption at the Cu-MgO interface compared to the Cu-ZnO interface. Cu₁₃/MgO/ZnO (100) surface model is studied to understand the promoting effect of MgO on CO₂ adsorption.

1. Introduction

Major industrialized nations are now more committed than ever to drastically reducing greenhouse gas emissions after the Paris agreement on Climate change. The Paris agreement's main goal is to limit global warming to well below 2 °C, preferably to 1.5 °C, compared to pre-industrial levels. Carbon dioxide (CO₂) is a greenhouse gas and emitted as a by-product from power plants, steel industries, oil refineries, chemical industries, and other energy production processes. Thus, excessive anthropogenic CO₂ emission led to climate change and global warming, which is one of the biggest problems nature and humanity is facing in the 21st century [1,2]. Concurrently, CO₂ is a high potential, cheap, non-toxic, and abundant C1 feedstock that can be utilized for the synthesis of fuels and value-added products. The catalytic transformation of carbon dioxide into valuable products like methanol, ethanol, syngas (CO + H₂), dimethyl ether (DME), urea, formaldehyde, carbonates, and hydrocarbons are the most attractive

ways that may offer a solution to utilize CO₂ and thereby mitigate its emission into the natural environment [2]. Because of the high thermodynamic stability of CO₂, the successful utilization of CO₂ is a real challenge, and selective catalytic hydrogenation of CO₂ into methanol has attracted appreciable attention as one of the possible paths for CO₂ fixation. Methanol can be used as a fuel (such as in methanol fuel cell), as a fuel additive (such as gasoline additive or MTBE production), or as an initial feedstock in the chemical industries (mainly downstream processes), and as a hydrogen supplier in direct methanol fuel cell (DMFC) [3].

Researchers around the world have been exploring different catalytic pathways like photocatalysis, electrocatalysis, and thermal heterogeneous/homogeneous catalysis for the utilization of CO₂ [2,4]. The main obstacle of CO₂ hydrogenation to methanol and other value-added chemicals by thermal heterogeneous catalysts is reverse water gas shift (RWGS) reaction [3] because the copper-based catalyst used in the methanol synthesis may also favour the RWGS reaction

* Corresponding author.

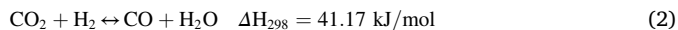
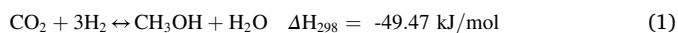
E-mail address: raja@iip.res.in (R. Bal).

<https://doi.org/10.1016/j.apcata.2021.118239>

Received 2 March 2021; Received in revised form 30 May 2021; Accepted 1 June 2021

Available online 4 June 2021

0926-860X/© 2021 Elsevier B.V. All rights reserved.



From the above two equations, it can be observed that with increasing temperature, the RWGS (Eq. (2) shown above) reaction becomes predominant. So, hydrogenation of CO_2 to methanol should be carried out at lower temperatures. Industrially methanol is produced from synthesis gas mixture over Cu/ZnO/ Al_2O_3 catalyst. The commercial Cu-Zn-Al-based methanol synthesis catalysts from syn-gas were also used for the production of methanol from pure CO_2 , but the selectivity is poor due to the formation of excess CO and methane [5–7]. Although several research groups found that Cu-Zn-Zr catalysts are effective for the production of methanol from CO_2 hydrogenation [4,8,9], but the industrial application is far away due to poor selectivity and rapid deactivation due to the sintering of Cu particles [10–12]. ZnO appears to be an important component as it prevents the agglomeration of Cu particles leading to the high Cu surface area required for methanol production [11,12]. It is reported that graphitic like ZnOx over-layers on Cu nanoparticles is the active site over the industrial Cu-Zn-Al catalyst [13]. When H_2 dissociates over metallic Cu hydrogen, spill-over is inevitable for high CO_2 conversion. So, to get high methanol selectivity, it is required to use a catalyst that can adsorb and activate CO_2 without breaking both the C–O bonds of the molecule [14]. For industrial Cu-Zn-Al catalysts, they do not cleave both bonds in the molecule, i.e., no methane formation, but the big problem is RWGS. High temperature increases the RWGS reaction, produces more CO, and results the decrease of selectivity of methanol. In order to increase the CO_2 conversion and to reduce the CO selectivity, the reaction is generally carried out at high pressure (> 50 bar) in industrial methanol production [15, 16]. The techno-economic analysis of this process was conducted, and it was found that the cost of the compressor to increase the system pressure is almost 45 % of the total equipment cost. The required energy consumption for compressing the gas is almost 66 % of the total electricity cost for the methanol plant [17]. So, from the industrial point of view, moderate pressure is economically favorable, but the performances of the Cu-based catalysts are very poor in terms of selectivity and stability at 30 bar and the temperatures below 277 °C [18–20]. Nakamura et al. [21] reported a six-fold increase in Cu/ZnO catalyst activity compared to the bare Cu surface for CO_2 conversion to methanol. They also reported that the exposed faces of Cu also play a pivotal role in CO_2 hydrogenation [21]. The same group also reported that the stability and activity of Cu-based ZnO catalyst are strongly associated with small Ga_2O_3 particles, which led to the formation of Cu^0 and Cu^{+2} species for the superior catalytic activity for CO_2 reduction to methanol [22]. It is also reported in the literature that H_2O produced during the CO_2 hydrogenation to methanol reaction accelerates the crystallization of Cu and ZnO, leading to catalyst deactivation [23]. It is also reported that high dispersion of Cu particles, which will be stable against sintering, is necessary to present on the catalysts [24,25]. Mureddu et al. [26] reported that ZnO plays an essential role in the Cu/ZnO catalyst because it inhibits the agglomeration and sintering of Cu nanoparticles and also leading a large surface area, which enhanced the activity of the catalyst for methanol formation. The strong synergy between Cu and ZnO has great inherent stability for CO_2 hydrogenation. It is generally accepted that the nanocrystalline metallic Cu species in catalysts are active phases for the reduction of CO_2 [27]. Researchers also reported that the conversion of CO_2 is affected by the metallic surface area, and the selectivity of methanol highly depends on the dispersion of basic sites on the catalyst surface [24,25]. So, the presence of high copper surface area and basicity of the catalyst is the key factors for selecting the methanol synthesis catalyst via CO_2 hydrogenation [28]. Alkaline-earth oxides are known as a solid base and also employed in different organic transformation reactions as a promoter or catalyst [29]. Additionally, the presence of alkaline earth oxide with the catalyst prevents agglomeration and increases the surface area of the catalyst [30]. Dasireddy et al.

[31] reported the significant role of alkaline-earth metal oxide (MgO, BaO, SrO, and CaO) on the copper-based catalyst, which enhanced the number of CO_2 and H_2 adsorption active sites and also increased the metal-support interaction with high metallic Cu surface area. There are reports that MgO inhibits RWGS reaction [32,33], so a catalyst with properties of inhibiting RWGS reaction and capable of CO_2 activation at low temperatures could be ideal for methanol formation via CO_2 hydrogenation. MgO as a catalyst component could lead to higher CO_2 adsorption because of its basic nature and also improve metal dispersion by increasing surface area due to its low density [33]. Different parameters like particle size, surface area, Cu surface area, and composition of the catalyst influence the catalytic activity and methanol selectivity in a CO_2 hydrogenation reaction. Although there are several reports in the literature for the catalytic hydrogenation of CO_2 to methanol over Cu based catalysts applying different preparation methods but to the best of our knowledge, there is no report till date where a Cu-based catalyst is showing very high selectivity and stability for a longer run. So, the development of highly stable and selective catalysts is highly inevitable.

Here, we report the highly dispersed sinter resistant Cu-nanoparticles supported on MgO-ZnO catalyst prepared by hydrothermal method, and the catalyst showed superior activity and > 99 % methanol selectivity at low temperature (200 °C) and low pressure (30 bar).

2. Experimental

2.1. Catalyst preparation

MgO promoted 5 wt% Cu on ZnO catalysts were synthesized by the hydrothermal method. A typical synthesis process for 20 (wt.%), MgO promoted Cu/ZnO catalyst is as follows: 1.8 g of low molecular weight poly (diallyldimethylammonium chloride) (PDADMAC), and 1.07 g cetyltrimethylammonium bromide (CTAB) dissolved in 20 mL water by vigorous stirring. Then 13.7 g $\text{Zn}(\text{NO}_3)_2 \cdot 6\text{H}_2\text{O}$ and 6.3 g of Mg $(\text{NO}_3)_2 \cdot 6\text{H}_2\text{O}$ of the precursor salts were dissolved in 80 mL water, and the mixing solution was added dropwise to the polymer solution. The whole solution mixture was stirred continuously for 2 h, and 0.9 g Cu $(\text{NO}_3)_2 \cdot 2.5\text{H}_2\text{O}$ dissolved in 10 mL water was added to the final mixture solution. Na_2CO_3 (2 M) solution was used as a precipitant and maintained the pH of the solution around 9–10 with vigorous stirring for 2 h continuously. After complete precipitation, the resulting solution was put into a Teflon-lined stainless-steel autoclave and treated for 24 h at 180 °C in an oven. After cooling down to room temperature, the product obtained after filtration were sequentially washed with distilled water to remove ions possibility of the remnant in the products. Finally, the catalyst was dried at 110 °C overnight and further calcined at 450 °C in the air for 6 h with a 1 °C/minute ramping rate. The catalyst is designated as CMZ-X^{HT}, where X (5, 10, 15, and 20) is the weight % of MgO in the catalyst.

2.2. Catalyst characterization

The catalyst was characterized by XRD, N_2 -physisorption, ICP-AES, XPS, SEM, HR-TEM, TPR, Pulse Chemisorption, EXAFS, and N_2O titration techniques. The details of characterization methods are given in the supporting information (Table S1).

2.3. Catalytic activity test

The activity measurement of the CO_2 to methanol transformation reaction over the synthesized catalysts was carried out in a continuous downflow fixed bed high-pressure reactor (Fig. 1), where typically 0.5 g catalyst (40–60 mesh) was mixed with 1.0 g porcelain bead, which was placed at the halfway point of a 7.92 mm stainless steel tube reactor between two quartz wools. The temperature of the furnace was

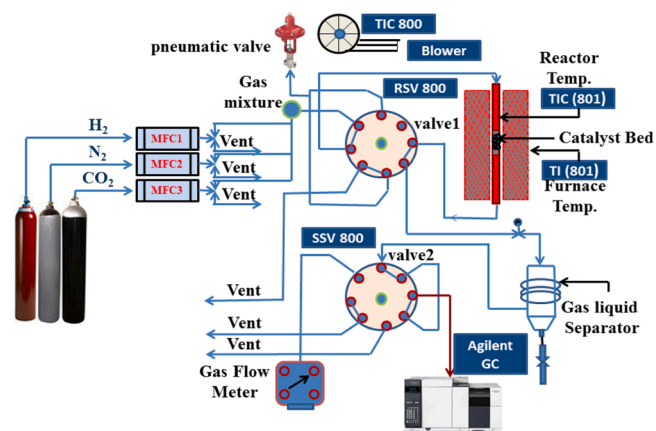


Fig. 1. Schematic diagram of continuous fixed bed reactor set-up for methanol production from CO₂ hydrogenation.

measured by a thermocouple fitted in the middle of the furnace, and also, the temperature of the reactor was measured by the thermocouple exposed to the thermowell at the bottom of the reactor (Supporting information). At the beginning of the reaction, the catalyst was initially reduced (heating rate 2 °C/min) in the presence of 10 % H₂ balanced He gas at 350 °C for 2 h under atmospheric pressure condition. After the reactor was cooled down to reaction temperature, the feed mixture (H₂: CO₂: N₂ = 3:1:1) with the total gas flow 60 mL/min) was introduced into the reactor, maintaining the weight hourly space velocity (WHSV) of 7200 mL_{g_{cat}}⁻¹ h⁻¹ and reaction pressure of 30 bar. Kinetic analysis of the reaction was carried out between the temperature range of 200–300 °C. The products were analyzed using online GC (gas chromatography, Agilent 7890A) fitted with two detectors thermal conductivity detector (TCD) and flame ionization detector (FID) using porapack-Q column (for analyzing H₂, N₂, CO, CO₂, and H₂O), and HP-Plot Q (for analyzing CH₃OH, CH₄, and other hydrocarbons).

The CO₂ conversion and product selectivity for CH₃OH, CH₄, and CO data were calculated by both internal standard normalization and mass-balanced method. The carbon balanced and material balance was conducted with an accuracy of ±3% in between 97%–103 %. The conversion of CO₂ (X_{CO₂}) and the selectivity of CH₃OH (S_{CH₃OH}) were determined based on the following equations:

$$X_{CO_2} = \frac{F_{CO_2, in} - F_{CO_2, out}}{F_{CO_2, in}} \times 100\% \quad (3)$$

$$S_{CH_3OH} = \frac{F_{CH_3OH, out}}{F_{CO_2, in} - F_{CO_2, out}} \times 100\% \quad (4)$$

3. Result & discussion

3.1. Characterization

3.1.1. Physicochemical properties and N₂ physisorption study

The estimation of Cu was examined by ICP-AES, and the results are given in Table S2, supporting information. BET surface area analysis by N₂ adsorption-desorption of the prepared catalysts is also provided in Table 1. The surface area of the support ZnO (ZnO^{HT}) synthesized by the hydrothermal method in the presence of CTAB and PDADMAC showed a surface area value of 50.3 m²/g. The surface areas of the Cu/ZnO^{HT} catalyst prepared by the hydrothermal method were 52.8 m²/g (Table 1). With the addition of MgO, Cu particles size decreases and dispersion increases, so surface to volume ratio of the catalyst increases, and the catalyst showed higher surface area. The specific surface area of the CMZ^{HT} catalyst was increased with increasing MgO loading, and it follows the order: CMZ-20^{HT} > CMZ-15^{HT} > CMZ-10^{HT} > CMZ-5^{HT} (Table 1). Copper surface area (S_{Cu}) determined by N₂O titration method

Table 1

Physicochemical properties of different catalysts.

Catalyst	Surface area ^a (m ² /g)	Metal Dispersion (MD; %)	Cu surface area (After calcination)	Cu particle size d _{Cu} (nm)	Number of the active Cu atoms /g
ZnO ^{HT}	50.3	ND	NA	NA	NA
CM ^{HT}	41.2	35.7	11.4	7.3	12.4
CZ ^{HT}	52.8	43.2	13.3	9.8	14.7
CMZ-5 ^{HT}	54.3	46.8	16.6	13.7	19.0
CMZ-10 ^{HT}	57.8	50.4	18.8	15.8	21.3
CMZ-15 ^{HT}	60.4	57.7	22.5	19.3	24.2
CMZ-20 ^{HT}	64.2	62.6	29.5	29.1	30.2

NA: Not available; and ND- Not determined.

^a N₂ physisorption method.

^b N₂O decomposition method using Cu metal dispersion.

is also presented in Table 1. CZ^{HT} catalyst shows the S_{Cu} of 14.7 m²/g, and the Cu dispersion was 13.3 %. With the addition of MgO, dispersion of Cu particles and copper surface area (S_{Cu}) increases, and CMZ-20^{HT} (MgO = 20 wt%) catalyst showed maximum S_{Cu} value of 30.2 m²/g. The increase in copper surface area (S_{Cu}) with the addition MgO may be due to the low density of MgO and the formation of small Cu species [33,34]. The variation of Cu dispersion (D_{Cu}) also showed a similar trend with the addition of MgO, and it is the inverse trend of the Cu particle size (d_{Cu}) measured by N₂O titration. The maximum Cu dispersion value of 29.5 % was obtained in the CMZ-20^{HT} catalyst. The Cu-specific surface area and Cu dispersion of the CMZ-20^{HT} catalyst are higher compared to the other catalysts (CMZ-15^{HT}, CMZ-10^{HT}, CMZ-5^{HT}, CZ^{HT}, and CM^{HT}). Several studies also supported the observation of increasing surface area with increasing metal loading [33–35].

3.1.2. Metal dispersion

The N₂O decomposition analysis was carried out to calculate the Cu dispersion, an average number of copper species present on the catalyst surface, copper surface area, and the results are tabulated in Table 1. From the analysis, it was observed that the dispersion of copper species markedly depends on both the amount of magnesium loading and the preparation method. The catalysts synthesized by the hydrothermal method exhibited higher dispersions, presence of smaller copper particles with high copper surface area. The addition of CTAB as a morphology controlling agent and PDADMAC as the size controlling agent produces very small, highly dispersed copper particles supported on nanocrystalline MgO-ZnO compared to the catalyst prepared in the absence of MgO. Copper dispersion increases with increasing the MgO loading over the Cu/ZnO catalyst. The CM^{HT}, CZ^{HT}, CMZ-5^{HT}, CMZ-10^{HT}, CMZ-15^{HT}, and CMZ-20^{HT} catalysts showed Cu dispersion values of 11.4 %, 13.3 %, 16.6 %, 18.8 %, 22.5 % and 29.5 %, respectively. The number of active particles presents estimated from metal dispersion analysis is reported in Table 1. It was found that the specific surface area (64.2 m²/g) was highest for CMZ-20^{HT}, and the number of active Cu atoms present on the catalyst is 3.06 × 10¹⁷ Cu atoms/g_{cat}. The number of active Cu atoms present on other catalyst are 1.58 × 10¹⁶, 5.82 × 10¹⁶, 6.78 × 10¹⁶ and 7.92 × 10¹⁶ Cu atoms/g_{cat}, respectively for CZ^{HT}, CMZ-5^{HT}, CMZ-10^{HT}, CMZ-15^{HT}. The number of active Cu atoms increases with increasing MgO loading, and the number of active Cu atoms present on the CMZ-20^{HT} catalyst is higher (3.06 × 10¹⁷ Cu atoms/g_{cat}) compare to the other catalysts. We have also measured the Cu dispersion

using N_2O titration method of the spent Cu/MgO/ZnO catalysts. N_2O titration method of the spent CMZ-20^{HT} catalyst was found that Cu dispersion (29.1 %) was almost same as that of the fresh CMZ-20^{HT} catalyst which confirms that the Cu particles present in the catalyst are very stable during CO_2 hydrogenation reaction. On the other hand, spent CM^{HT}, CZ^{HT}, CMZ-5^{HT}, CMZ-10^{HT} and CMZ-15^{HT} catalysts showed lower Cu dispersion (7.3, 9.8, 13.7, 15.8 and 19.3 %) compare to the fresh CMZ-20^{HT} catalyst and this may be the reason for the deactivation of this catalyst during CO_2 hydrogenation reaction (Table 1).

3.1.3. X-ray diffraction (XRD)

Crystallinity of the prepared catalysts was analyzed by powder XRD, where all the synthesized samples showed very high crystallinity. The CZ^{HT} and CM^{HT} catalysts showed the characteristic peaks for ZnO and MgO, respectively, and also a peak at 38.72° , which is assigned for CuO (JCPDS Card no. 89-5896). CMZ-5^{HT}, CMZ-10^{HT}, and CMZ-15^{HT} catalysts also showed the characteristic peaks for CuO peaks at 38.72° for CuO species using Scherrer's equation (Table S3, supporting information), whereas it was also found that the fresh CMZ-20^{HT} catalyst did not show any peak of Cu-species, indicating that the catalyst might contain very small Cu-species (< 5 nm), which was not detected by XRD (Fig. 2A) [36,37]. The observation also indicates that CuO species have a strong interaction with ZnO crystals in the presence of MgO, which led to the high dispersion of Cu throughout the catalyst surface, forming very small Cu-species [38,39].

With the increasing of MgO loading, it was observed that the intensity of the XRD peaks for MgO was increasing, and it was also influencing the intensity of ZnO peaks. It was revealed that the addition of a small amount of MgO in the catalyst influencing the exposed planes of the ZnO crystals. The peak at a 2θ value of 34.44° for ZnO in the synthesized CMZ-X^{HT} catalysts is shifted to a higher value. It was also observed that the peak at a 2θ value of 34.39° for ZnO in the CZ^{HT} catalyst shows the normal value as the JCPDS value. So, in the case of CMZ-X^{HT} catalysts, ZnO lattice size decreased (shown in Table S2, Supporting information) as Mg atoms partially replaced Zn atoms in the ZnO crystals [40]. We observed that there is a formation of a solid solution between ZnO and MgO, which highly influences the catalytic activity, showing very high methanol selectivity for the CMZ-X^{HT} catalysts. The unit cell parameter value 'a' of the ZnO lattice decreases from normal value 0.3507 nm to 0.3505 nm after substitution of Zn^{2+} ion ($r_{Zn^{2+}} = 0.088$ nm) by small Mg^{2+} ion ($r_{Mg^{2+}} = 0.086$ nm), which is in agreement with the Vegard's rule.

XRD patterns of all the spent catalysts are shown in Fig. 2B, where except the CMZ-20^{HT} catalyst, all other catalysts indicated the presence

of metallic Cu particles. XRD peak at 2θ value of 50.45° are corresponding to metallic Cu (JCPDS Card no. 89-2838). The absence of XRD peaks for any copper species for CMZ-20^{HT} catalyst indicates that most probably highly dispersed Cu-species (< 5 nm) [36,37] are present, and the size of the Cu species also remains unaffected during catalysis. The observation also revealed that the interaction of the metal with support present in the CMZ-20^{HT} catalyst also played a vital role in preventing the agglomeration of the Cu-species and maintained its size to < 5 nm during the catalysis.

3.1.4. SEM analysis

The morphology of the prepared CMZ-20^{HT} catalyst was carried out by SEM analysis. As shown in Fig. 3A, the CMZ-20^{HT} catalyst showed platelet like morphology, which can be seen on the surface of microspherical species. The catalyst showed a uniform distributed morphology with a particle size between 20–70 nm. The observations also indicated the strong metal-support interaction between Cu-nanoparticles on supported MgO/ZnO catalyst. The morphology of the spent catalysts was also examined by the SEM analysis, which is shown in Fig. 3B. The spent CMZ-20^{HT} catalysts exhibited almost unchanged morphology after reaction catalysts, which showed thermal stability.

3.1.5. TEM analysis

Morphological properties of the synthesized catalysts were carried out by doing TEM analysis, and Fig. 4 represents the TEM images of fresh and used (spent) CMZ-20^{HT} catalysts. Fig. 4a–e show the overall morphological image of the fresh CMZ-X^{HT} catalyst. The fresh CMZ-20^{HT} catalyst showing the size of the CuO particles ~ 5 nm. The lattice fringes with d-spacing values of 2.32 Å and 2.47 Å, corresponding to CuO (111) and ZnO (101) planes, respectively, can also be seen in Fig. 4e. It is clear from the TEM images that the morphology of the spent catalyst is almost the same as that of the fresh catalyst, and the lattice fringes with d-spacing values of 2.32 Å for CuO (111) and 2.08 Å for metallic Cu (111) planes for the spent catalysts can also be seen in Fig. 5e. The presence of both metallic Cu and CuO species in the fresh and spent CMZ-20^{HT} catalysts also supported by the XPS and EXAFS analysis (discussed later). The observation from TEM analysis revealed that the CMZ-20^{HT} catalyst is very stable against sintering, and the Cu particle size remains ~ 5 nm during CO_2 hydrogenation. On the other hand, the Cu catalyst prepared hydrothermally on supported ZnO (CZ^{HT}) showed agglomerated particles for the fresh catalyst as well as for the spent catalysts (Fig. 5a). This could be due to larger Cu-species particles with lower metal-support interactions, and these Cu particles are not stable under reaction temperature and pressure [41,42]. The TEM images of the different fresh

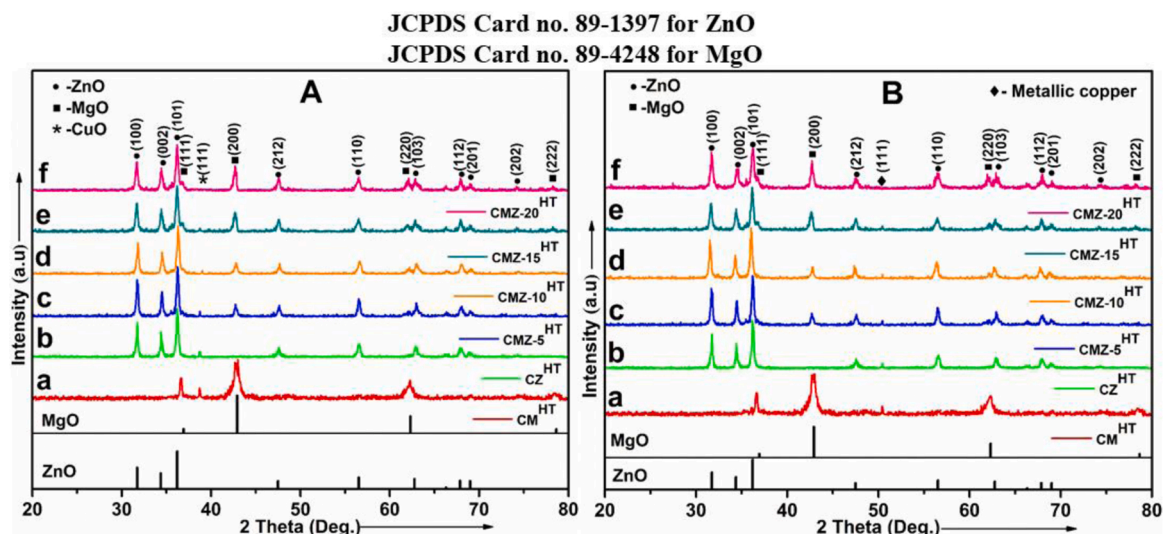


Fig. 2. Powder XRD patterns of (A) fresh (After calcination) and (B) Spent catalysts.

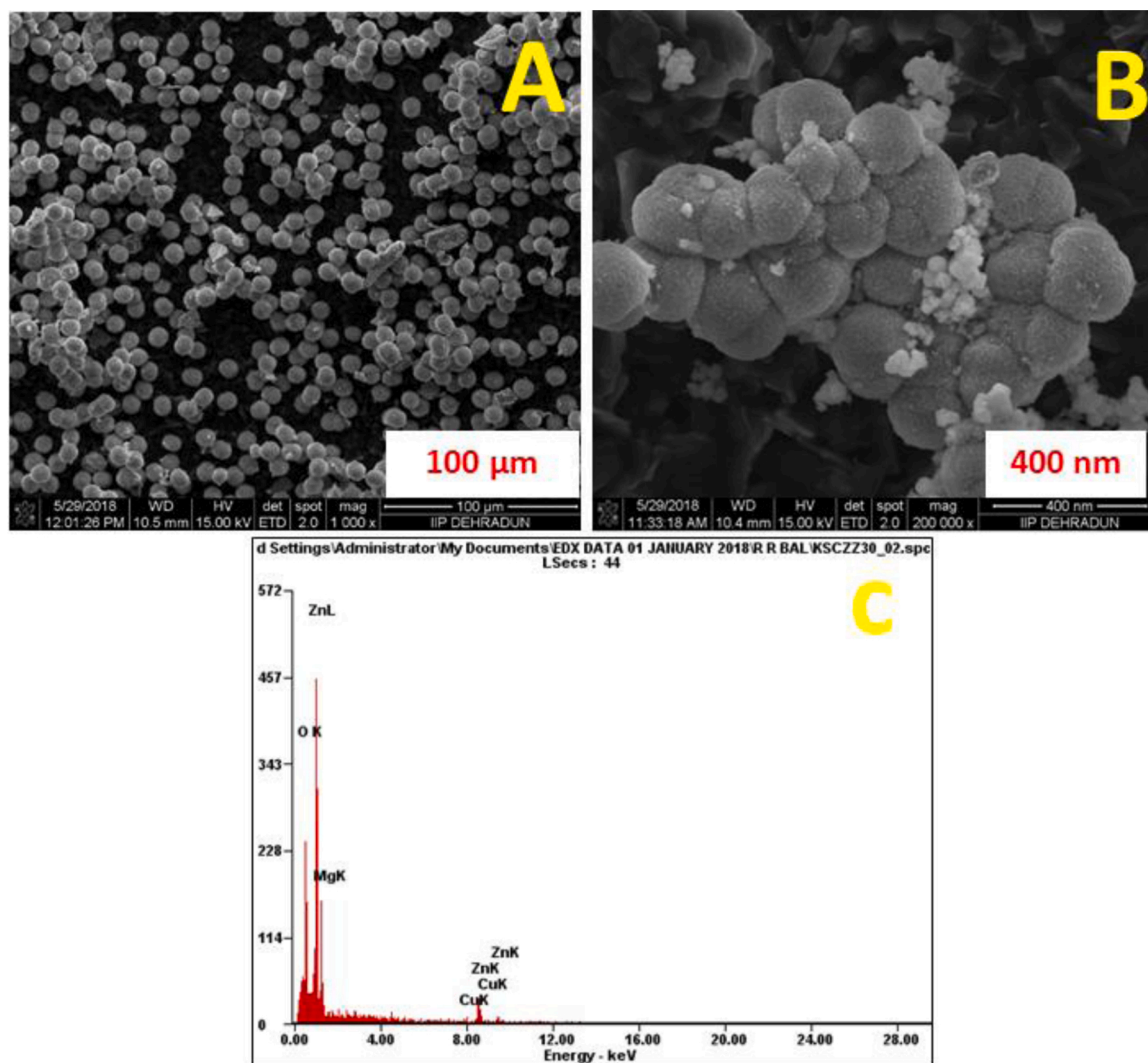


Fig. 3. SEM images (A) fresh (After calcination), (B) spent and (C) EDS analysis of CMZ-20^{HT} catalyst.

and spent catalysts (CMZ-5^{HT}, CMZ-10^{HT}, and CMZ-15^{HT}) exhibited mostly the agglomerated particles, as shown in Fig. 5 (5b, 5c and 5d). The Cu dispersion on nanocrystalline MgO/ZnO was determined by the elemental mapping of nanostructured catalysts, indicating a homogeneous dispersion of Cu on the nanocrystalline MgO/ZnO support (Fig. S1, supporting information).

3.1.6. Structure-activity correlations

Structure-activity correlations were established by using the steady-state activity (time on stream 3 h) data. It is evident that the activity is strongly correlated with the copper surface area and Cu particle size (shown in Fig. 6A and B). It was observed that catalysts with high Cu surface area as well as high Cu dispersion exhibited with very high methanol production rate. Cu surface area and dispersion followed the order: CMZ-20^{HT} (S.A. = 30.2 m²/g, dispersion = 29.5) > CMZ-15^{HT} (S.A. = 24.2 m²/g, dispersion = 22.5) > CMZ-10^{HT} (S.A. = 21.3 m²/g, dispersion = 18.8) > CMZ-5^{HT} (S.A. = 19.0 m²/g, dispersion = 16.6) > CZ^{HT} (S.A. = 14.7 m²/g, dispersion = 13.3) > CM^{HT} (S.A. = 12.4 m²/g, dispersion = 11.4) and the methanol production rate also followed the same order: CMZ-20^{HT} (0.0063 mol g_{Cu}⁻¹ h⁻¹) > CMZ-15^{HT} (0.0052 mol g_{Cu}⁻¹ h⁻¹) > CMZ-10^{HT} (0.0050 mol g_{Cu}⁻¹ h⁻¹) > CMZ-5^{HT} (0.0045 mol g_{Cu}⁻¹ h⁻¹) > CZ^{HT} (0.0033 mol g_{Cu}⁻¹ h⁻¹) as shown in Fig. 6A. Earlier researchers also observed a similar linear correlation between Cu surface area and activity over different metal oxide support [43–46]. In addition,

the dependence of the methanol production rate of all the catalysts on copper particle size is shown in Fig. 6B, where a high methanol production rate was achieved with smaller Cu particles. The CZ^{HT}, CMZ-5^{HT}, CMZ-10^{HT}, CMZ-15^{HT}, CMZ-20^{HT} catalysts showed the methanol production rates of 0.0033, 0.0045, 0.0050, 0.0052 and 0.0063 mol g_{Cu}⁻¹ h⁻¹, and the Cu particles size was 7.2, 5.6, 4.9, 4.7 and 3.5 nm respectively.

In general, the properties of low-index (110) and (100) planes, corners, edges are influenced by Cu particle size, which in turn influences both surface structure and electronic properties [47]. Low-index facets get primarily exposed by the surface of larger particles, with fewer edge or defect sites [48]. On the other hand, a larger number of open planes, edge/defect sites with coordinately unsaturated atoms are present in smaller particles. Hence, they are more reactive than fully coordinated species. We believe that in our case, the activity of the Cu/ZnO catalyst promoted with MgO is superior since low coordinated Cu-atom sites of smaller nanoparticles are present. These sites stabilize HCOO, H₂COO, H₂CO, key intermediates species of the CO₂ reduction process. This kind of interaction and stabilization of these species lowered the activation energy barrier for the hydrogenation step. Smaller Cu particles will also have more interfacial area with supported metal oxide, indicating that metal-support interaction may also play a crucial role during catalysis.

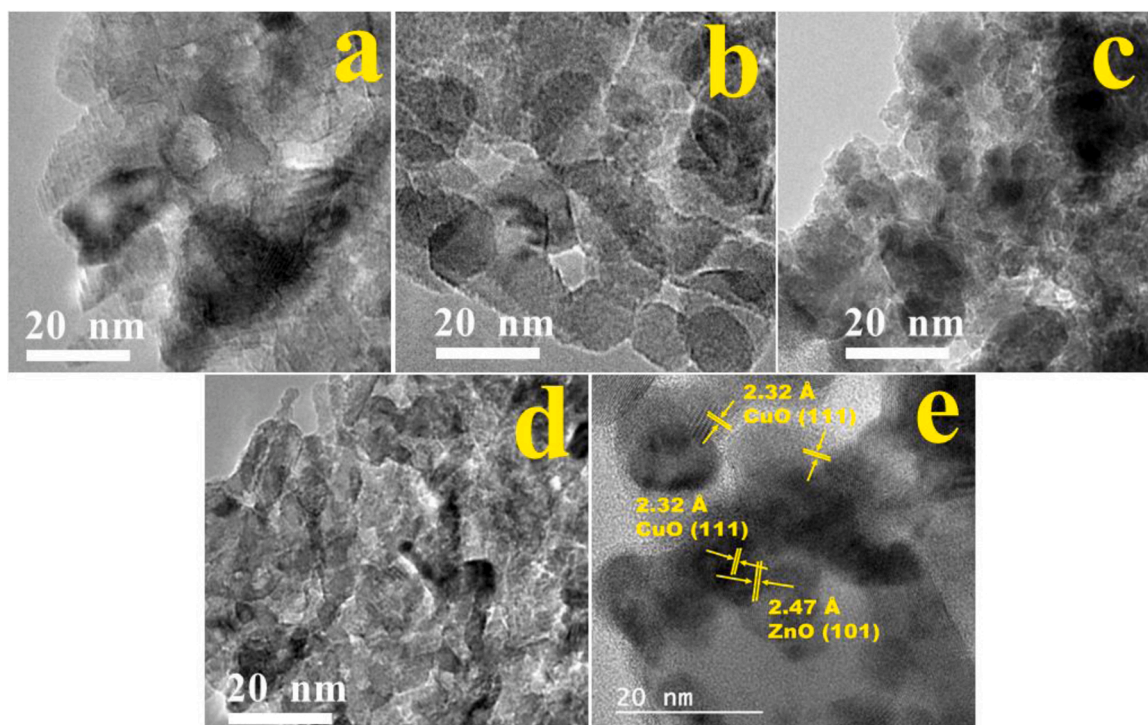


Fig. 4. TEM images of fresh (After calcination) (a) CZ^{HT}, (b) CMZ-5^{HT}, (c) CMZ-10^{HT}, (d) CMZ-15^{HT}, and (e) CMZ-20^{HT} catalysts.

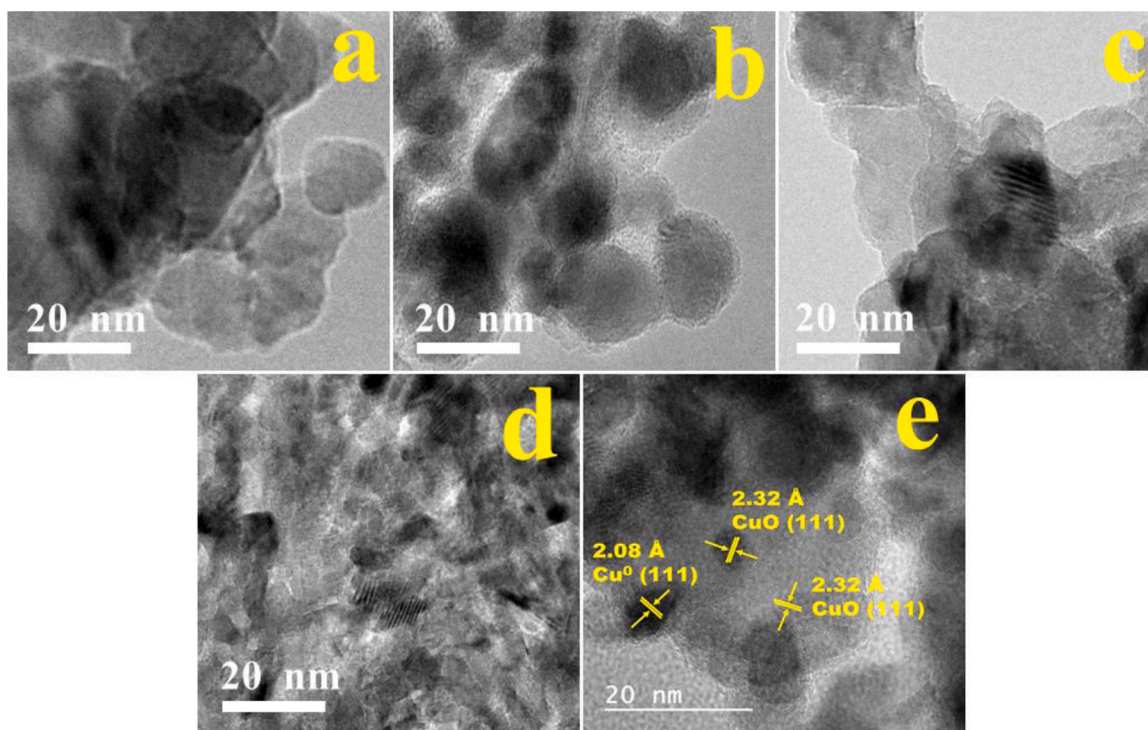


Fig. 5. TEM images of spent (a) CZ^{HT}, (b) CMZ-5^{HT}, (c) CMZ-10^{HT}, (d) CMZ-15^{HT}, and (e) CMZ-20^{HT} catalysts.

3.1.7. H₂-TPR analysis

Reducibility of the synthesized catalysts was tested by H₂-TPR analysis (Fig. 7). All the catalysts showed similar kinds of reduction patterns with the differences in reduction temperatures (T_{\max}). Cu-oxide species in the CMZ-20^{HT} catalyst were reduced at the lowest temperature (T_{\max} = 220 °C), indicating that the catalyst has the smallest Cu-oxide particles that exist on the surface of the ZnO support amongst

the synthesized catalysts [49,50]. T_{\max} for different catalysts follows the order: CMZ-20^{HT} (T_{\max} : =220 °C) < CMZ-15^{HT} (T_{\max} : =232 °C) < CMZ-10^{HT} (T_{\max} : =237 °C) < CMZ-5^{HT} (T_{\max} : =242 °C) < CZ^{HT} (T_{\max} : =251 °C) < CM^{HT} (T_{\max} : =268 °C), so the Cu particle size also follows a similar order [51]. It can be observed that all the catalysts showed board Cu reduction peaks, and these reduction peaks could be due to the presence of larger Cu-oxide nanoparticles with different sizes at the

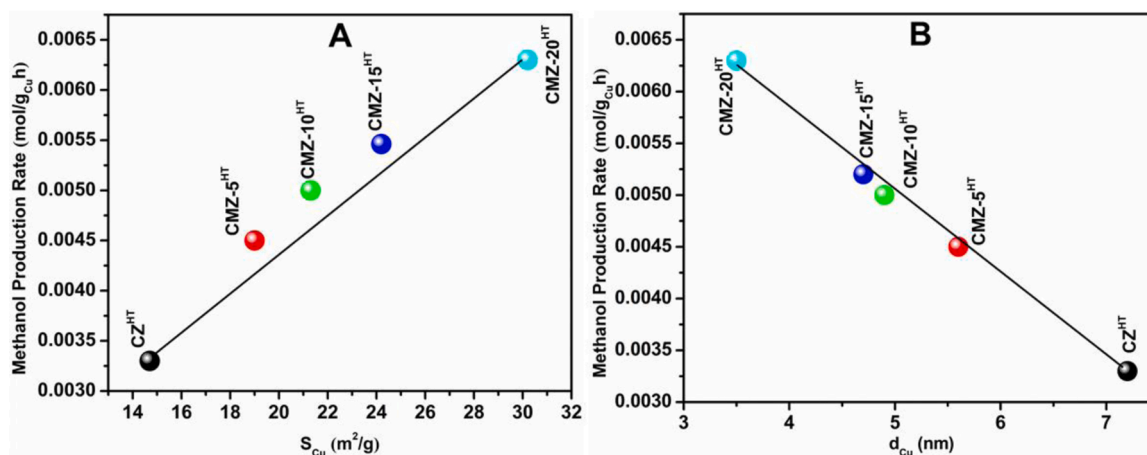


Fig. 6. (A) Correlations between methanol formation rate and copper surface area and, (B) Correlations between methanol formation rate and Cu particle size over the catalysts.

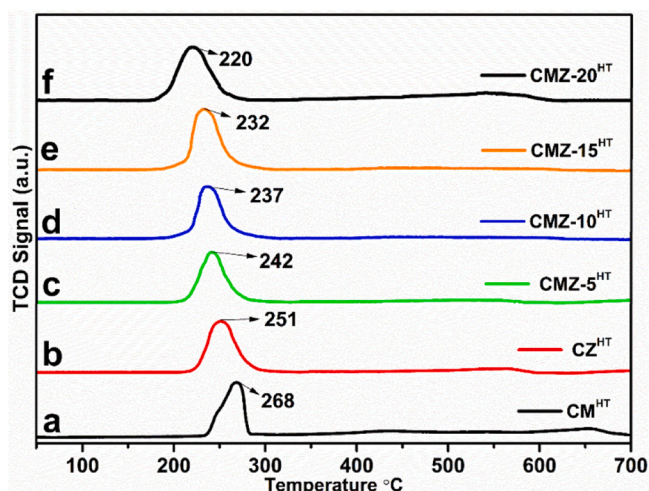


Fig. 7. H₂-TPR patterns of fresh (After calcination) catalysts.

surface or encapsulated Cu-nanoparticles present in bulk [49], as the reduction of ZnO [52], and MgO is not possible by H₂ at this temperature range [53]. The Cu peak of CMZ-20^{HT} catalyst showed single reduction peaks at 220 °C, which revealed that the catalyst has smaller and well dispersed Cu-oxide particles, which are easily reducible. As the catalyst (CMZ-20^{HT}) does not contain large Cu particles (confirmed by HRTEM, high metal dispersion, and STEM elemental mapping analysis in Fig. S1), it indicates the presence of strong metal-support interaction (SMSI). Due to the presence of SMSI, the interface of the small active Cu and nanocrystalline ZnO-MgO support binds the reactive intermediates very strongly and reduced the activation energy barrier and shows superior activity. SMSI is the main driving force to keep the Cu particle size intact during catalysis by preventing against sintering in the presence of H₂, and the catalyst does not deactivate even after the 120 h time-on-stream test. It is also believed that the synergy between very small Cu-nanoparticles and nanocrystalline ZnO-MgO support also favours the high activity of the catalyst. The absence of SMSI or the presence of very weak metal support interaction over other catalysts (CZ^{HT}, CMZ-5^{HT}, CMZ-10^{HT}, and CMZ-15^{HT}) makes the Cu particles vulnerable for sintering (agglomeration) during catalysis in the presence of H₂ (Fig. 7). It has to be noted that the agglomeration of the metal nanoparticles is energetically favoured due to minimizing the surface areas by saturating the binding and co-ordination sites. It was found that the Cu particle size increases as agglomeration taking place (confirmed by TEM analysis)

during catalysis, and the activity decreases with time for all the catalysts except CMZ-20^{HT}. It was also found that the surface area of the spent catalyst also decreases over all the CMZ catalyst except CMZ-20^{HT}, indicating the sintering of the catalyst. So, in the case of CMZ-20^{HT}, SMSI plays a very vital role in stabilizing the very small Cu particles, and the interface between the Cu-particles and Mg-incorporated ZnO support (confirm from XRD analysis) facilitates the formation of reactive intermediates.

3.1.8. XPS measurement

X-ray photoelectron spectroscopic (XPS) analysis was carried out to examine the chemical state or oxidation state of Cu elements present on the fresh and spent catalysts. Both fresh and spent CMZ-5^{HT}, CMZ-10^{HT}, CMZ-15^{HT}, and CMZ-20^{HT} catalysts were analyzed, and comparative analysis of CZ^{HT} catalyst was also carried out (Fig. 8A and B). Fig. 8A exhibited the core level Cu2p XPS spectra of the fresh CZ^{HT} catalyst. Cu2p_{3/2} XPS peaks with binding energy values of 933.6 eV indicated CuO, and the binding energy value of 934.4 eV attributed to Cu(OH)₂ on the surfaces of fresh CZ^{HT} catalyst. However, the Fresh CMZ-20^{HT} catalyst showed characteristic peaks for Cu-species, and after deconvolution, two peaks at binding energy values of 932.7 eV and 933.8 eV were observed. The first peak is due to metallic Cu or Cu₂O, as both the species show very close binding energies [54,55]. EXAFS analysis of the fresh CMZ-20^{HT} confirms the presence of metallic Cu and Cu₂O (Table 2). Deconvolution of the XPS of spent CMZ-20^{HT} catalyst also showed two peaks at 932.2 eV and 933.3 eV, and these peaks are assigned for metallic Cu and CuO species, respectively. For comparison, XPS analysis of CZ^{HT} catalysts (fresh and spent) was also carried out, and it showed that the spent catalyst contains three types of Cu-species as Cu₂O (932.7 eV), CuO (933.6 eV), and Cu(OH)₂ (934.4 eV). For spent catalysts, the Cu 2p_{3/2} and Cu 2p_{1/2} peaks are followed by extended shake-up satellite appearance at 942 and 962 eV confirmed the presence of Cu²⁺ species [56]. These satellites were due to the charge transfer between the transition metal 3d and surrounding ligand oxygen 2p orbitals, and the absence of satellites in the spectra confirmed that no considerable quantity of Cu²⁺ species is left on the surface [56]. The Cu XPS spectra of the higher Cu loading fresh catalysts (CMZ-5^{HT}, CMZ-10^{HT}, and CMZ-15^{HT}) exhibited the presence of CuO and Cu(OH)₂, whereas the XPS spectra of spent catalysts showed the presence of metallic Cu and CuO and Cu(OH)₂ species, as shown in Fig. 8.

3.1.9. EXAFS analysis

EXAFS spectra of fresh and spent CMZ-20^{HT} catalysts are shown in Fig. 9A and B, respectively, and the curve fitting results of both catalysts are summarized in Table 2. For the fresh catalyst (Fig. 9A), EXAFS spectra exhibited the presence of Cu—O bond length of 0.1962 ± 0.0019

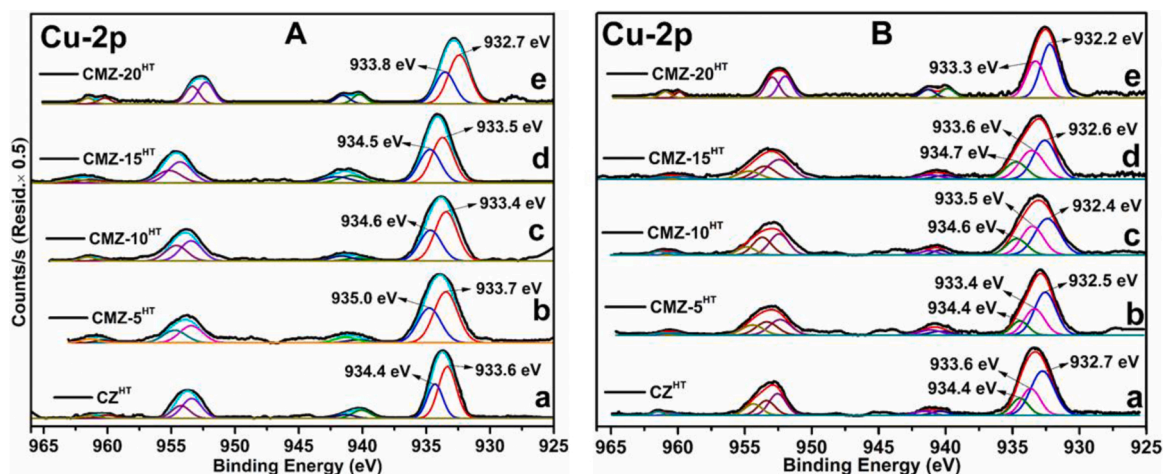


Fig. 8. XPS analysis of fresh (After calcination) (A) and (B) spent catalysts.

Table 2

Summary of fitted results for Cu k-edge EXAFS analysis.

Catalysts	Path	R (10^{-1} nm)	CN	DW(10^{-5} nm ²)	Δk (10 nm ⁻¹)	ΔR (10^{-1} nm)	ΔE_0 (eV)	R _f (%)
CMZ-20 ^{HT} fresh [#]	Cu-O	1.962 ± 0.019	2.1 ± 0.5	2.6 ± 2.2	2.0 – 11.0	1.2– 2.7	-1.4 ± 2.9	2.43
CMZ-20 ^{HT} spent	Cu-Cu	2.641 ± 0.046	6.5 ± 1.0	26.7 ± 3.9	1.0 (fixed)	1.2– 2.7	-9.9 ± 6.1	3.99
	Cu-O	1.905 ± 0.037	0.6 ± 0.4					
	Cu-Cu	2.554 ± 0.037	10.0 ± 3.0	14.5 ± 2.1				

*1: The reducing factor for Cu-O S_0^2 was assumed as 0.95. The reducing factor for metallic Cu phase S_0^2 was 0.694, determined by fitting with Cu foil data. [#]After calcination.

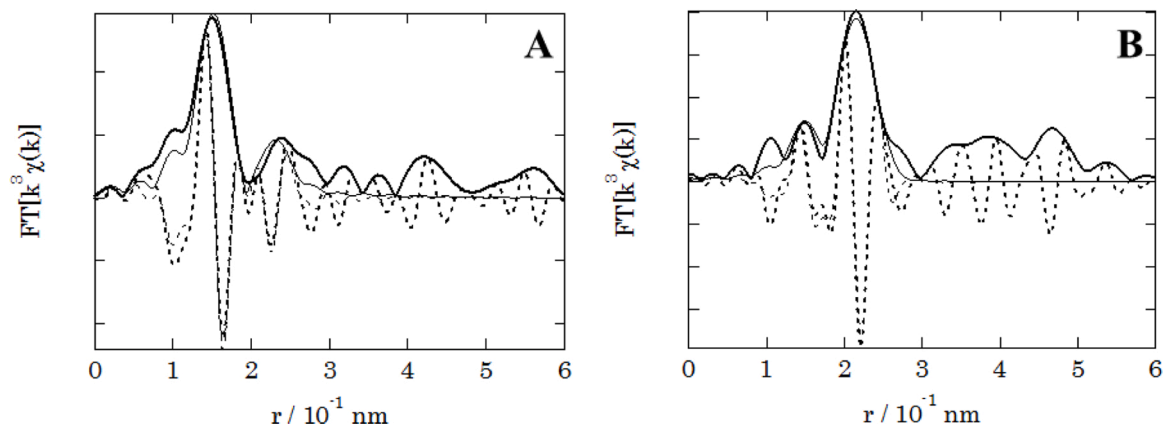


Fig. 9. k^3 -weighted Fourier transforms of Cu k-edge EXAFS for the (A) fresh (After calcination) CMZ-20^{HT} and (B) spent (After reaction) CMZ-20^{HT} catalyst. Imaginary and amplitude part is traced by dotted and solid curves, respectively. Ascertained data are indicated with solid lines, and fitting data are indicated with dotted lines.

nm with the co-ordination number of 2.1 ± 0.5 , which indicates the presence of Cu (II) species. The Cu—Cu bond length of 0.2641 ± 0.0046 with a co-ordination number of 6.5 ± 1.0 confirms the presence of metallic Cu species. These results also supported by the XPS analysis, EXAFS analysis for the spent catalysts showed the Cu—O bond length of 0.1905 ± 0.0037 nm with a coordination number of 0.6 ± 0.4 indicates the presence of Cu (II) species, whereas Cu—Cu bond length was 0.2554 ± 0.0037 with the coordination number of 10.0 ± 3.0 confirms the presence of metallic copper species (Fig. 9B). EXAFS analysis also confirms that the Cu species is stable during the CO₂ hydrogenation reaction.

4. Results and discussions

4.1. Catalyst activity

The activity of the CMZ-20^{HT} catalyst was measured at different reaction temperatures. The effect of temperature on CO₂ conversion, methanol selectivity, and yield was tested in the range of 200–300 °C, and it was found that CMZ-20^{HT} catalyst showed a continuous increase of CO₂ conversion with an increase in temperature. CM^{HT} and CZ^{HT} catalyst also showed conversion of CO₂ at 200 °C with 3.5 %, 5.5 % CO₂, and 66 %, 72 % methanol selectivity, respectively. CMZ-20^{HT} catalyst showed the 8.7 % CO₂ conversion with the methanol selectivity of ~100 %. From the reaction results, it is evident that the presence of both MgO and ZnO played a significant role in CO₂ activation and higher methanol

selectivity. The surface area of CZ^{HT} and CMZ-20^{HT} is 52.8 m²/g and 64.2 m²/g, respectively, and from XRD, it was observed that the size of Cu particles of CZ^{HT} is much larger (> 5 nm) than the size of Cu particles (~ 5 nm) in CMZ-20^{HT}. Metal dispersion analysis of CMZ-20^{HT} catalyst also revealed the presence of Cu particles with size ~ 3.5 nm and for CZ^{HT} catalyst, it is ~ 7.2 nm. The influence of Cu crystallite size indicates that the CO₂ transformation to methanol reaction over MgO promoted Cu-ZnO is structure sensitive. The addition of Mg increases the strain in the ZnO lattice is also responsible for the higher activity. The increase in rates with smaller Cu crystallites may be attributed to the higher number of exposed crystal planes, edges/corners/defect sites present in the catalyst, which contains co-ordinately unsaturated atoms, which are responsible for lowering the activation energy by strongly binding the reactive intermediates. The incorporation of MgO improved the Cu dispersion of the CMZ-20^{HT} catalyst. However, it did not increase the total surface area of the catalyst, which is the key factor in showing the high activity of the catalyst. The Cu surface area measured by the N₂O decomposition method was 30.2 m²/g for the CMZ-20^{HT} catalyst, which is very high compared to the other catalysts (Table 1). The number of active Cu atoms presents in the CMZ-20^{HT} catalyst (3.06×10^{17} Cu atoms/g_{cat}) is also very high compared to the other catalyst (Table 1). With the presence of a very high Cu surface area and a number of active Cu atoms on the surface of CMZ-20^{HT}, this catalyst showed very good catalytic activity for CO₂ hydrogenation to methanol transformation with very high methanol selectivity and high catalyst stability. On the other hand, the low basicity of ZnO and the presence of larger Cu particles of CZ^{HT} is the reason for showing low activity of the CZ^{HT} catalyst. The addition of MgO to the Cu-ZnO catalyst improved the basic nature of the catalyst, where adsorption of CO₂ molecules increased. It is also reported that the interface between Cu and ZnO plays the most significant role for methanol formation from CO₂ over the Cu-ZnO catalyst [7,57–59]. In the case of CMZ-20^{HT} catalyst, the presence of

smaller Cu particles with high Cu dispersion and the presence of metal-support interaction increases CO₂ conversion and methanol selectivity compared to other catalysts. The effect of temperatures over other CMZ-^{HT} (CMZ-5^{HT}, CMZ-10^{HT}, and CMZ-15^{HT}) catalysts are shown in Fig. 10. It was observed that the conversion of carbon dioxide increases with increasing temperatures, as shown in Fig. 9A. It was also noticed that with increasing temperature, the CO selectivity increases, as shown in Fig. 9C. All the catalysts (CMZ-5^{HT}, CMZ-10^{HT}, CMZ-15^{HT}, and CMZ-20^{HT}) showed a higher CO formation with increasing the temperature due to the reverse water-gas-shift reaction (RWGS). It was observed that in the case of the CMZ-20^{HT} catalyst, there was no CO formation at 200 °C (Fig. 9C). So, we conclude that at low temperatures, the selectivity for methanol is higher. Sun et al. reported that the formation of higher CO as a by-product via reverse water gas shift reaction (RWGS) led to the moderate deactivation of the catalyst as CO acts as a reducing agent [60] Due to the higher reducing potential of CO, it can reduce the surface of ZnO supported particles. Cu is an active metal for promoting methanol production from CO₂, but the size of the copper particles plays an important role, which affects the catalyst activity [61, 62]. As the size of the active species increases, the reducibility decreases [49,50], which directly influences the methanol selectivity. For CMZ-20^{HT} catalyst, TEM images show the presence of Cu particles with size ~ 5 nm, but the Cu particle size calculated from metal dispersion analysis is ~3.5 nm. The difference in the active species particle sizes can be explained by the fact that in TEM images, only a portion of the catalyst is analyzed, and very small Cu particles were not detected by the technique. It was found that the strong metal-support interaction (SMSI) is present (confirmed by H₂-TPR) in the case of CMZ-20^{HT}, which resist the very small Cu-particles against sintering during catalysis, whereas the absence of SMSI for the other catalysts (CMZ-5^{HT}, CMZ-10^{HT}, and CMZ-15^{HT}) make the Cu particles easy to sinter in the presence of H₂ during catalysis.

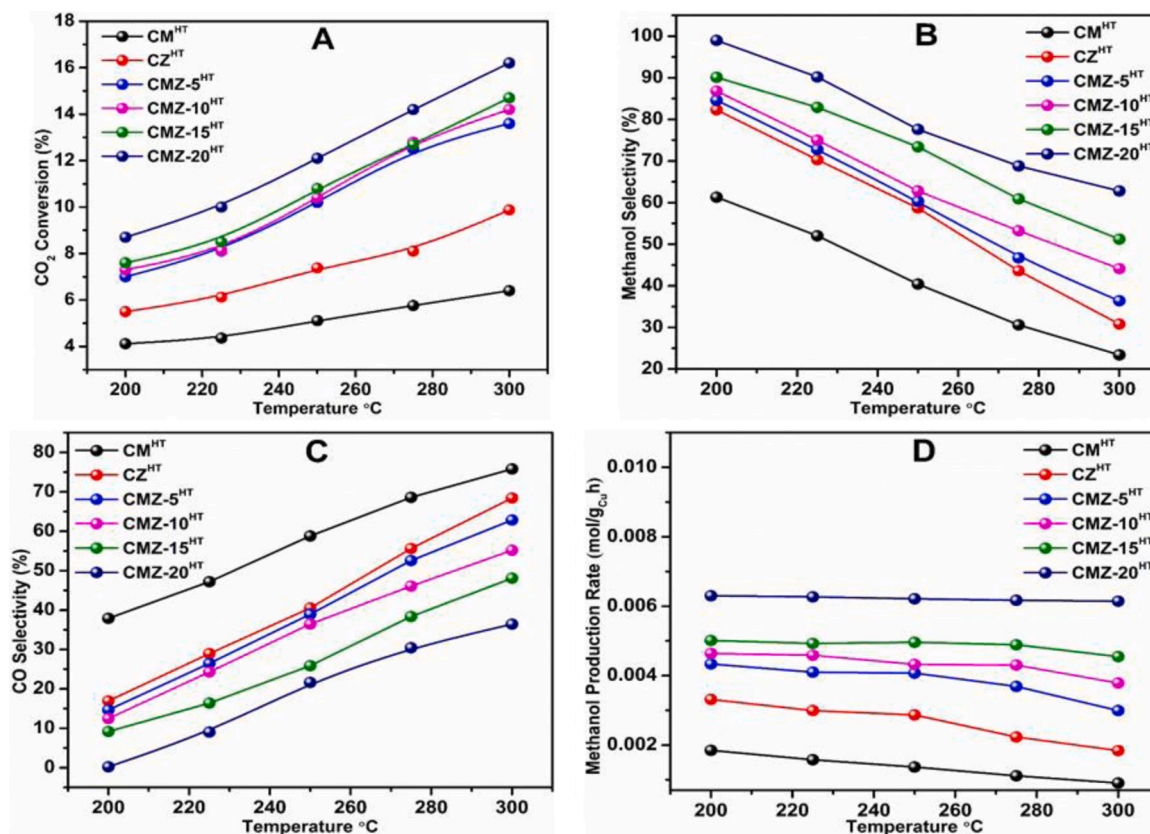


Fig. 10. Catalytic activity catalysts (A) CO₂ conversion, (B) CH₃OH selectivity, (C) CO selectivity, and (D) CH₃OH yield. Reaction Conditions: Temperature (200 °C), Pressure (30 bar), WHSV (7200 mL.g⁻¹.h⁻¹), Feed ratio (H₂: CO₂: N₂ = 3:1:1).

Time-on-stream study of the CMZ-20^{HT} catalyst is shown in Fig. 11, where this catalyst does not show any deactivation, whereas the CZ^{HT} catalysts deactivate very rapidly. The stability of the CMZ-20^{HT} catalyst arises due to the presence of strong metal-support interaction and the presence of small Cu particles with very high dispersion over ZnO support in the presence of MgO, which helps to inhibit the sintering of the catalyst, showing no deactivation. Whereas the absence of strong metal supports interaction, the presence of big Cu particles with low dispersion favours sintering for the CZ^{HT} catalyst, showing deactivation of the catalyst. CZ^{HT} catalyst loses almost 80 % activity after 120 h time-on-stream due to the sintering of Cu-particles during catalysis. TEM images and EXAFS analysis also support the fact that the size of Cu-particles remains constant for the CMZ-20^{HT}, whereas the particle size increases (agglomeration took place) in the case of the CZ^{HT} catalyst. In general, the deactivation of the copper-based catalysts occurred due to Cu sintering, decrease in catalytic reducibility, presence of excess surface hydroxyls, and absence of strong metal-support interaction. It was also found that the stability of the catalyst depends on active particle size, presence of high metal dispersion with a high surface area of the support (which also improves the dispersion of Cu-species). It is clear that the CMZ-20^{HT} catalyst is more stable during CO₂ hydrogenation compare to CMZ-5^{HT}, CMZ-10^{HT}, and CMZ-15^{HT} catalysts. The reason for the deactivation of these catalysts may be due to the sintering in Cu-species due to the absence of strong metal-support interaction.

4.1.1. DFT results

To understand the promotional effect of MgO in the Cu/ZnO catalyst, DFT calculations were performed to calculate the CO₂ adsorption energy over different model surfaces of the catalyst. The DFT optimized geometry of the ZnO(100) and MgO(100) surfaces were shown in Fig. 12. The Cu₁₃/ZnO(100) catalyst surface is obtained by adsorbing a Cu₁₃ nanocluster over the ZnO(100) surface, as shown in Fig. 13(a). The geometry optimized Cu₁₃/ZnO(100) surface shows a strong interaction between the ZnO(100) surface and the Cu₁₃ nanoparticle. Similarly, the Cu₁₃/MgO(100) catalyst surface is obtained by adsorbing a Cu₁₃ nanocluster over the MgO(100) surface, as shown in Fig. 13(b). The adsorption energy of the Cu₁₃ nanoparticle over the MgO(100) surface was found to be -2.1 eV, which is 0.6 eV higher compared to the ZnO(100) surface. Two more models of active catalyst surfaces, Cu₁₃/MgO/ZnO(100) and Cu-strip/ZnO(100), were shown in Figs. 13(c) and 11 (d), respectively. The Cu₁₃/MgO/ZnO(100) surface was obtained by adding

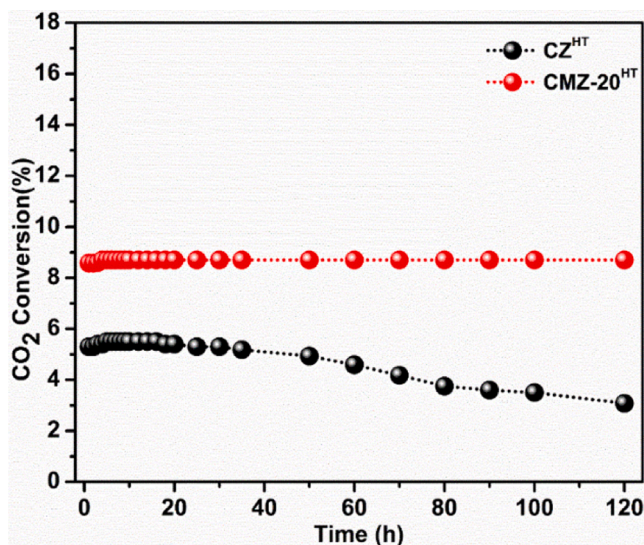


Fig. 11. Time on stream (TOS) results for CO₂ hydrogenation to methanol. Reaction Condition: Weight of Catalyst (0.5 g), Temperature (200 °C), Pressure (30 bar), WHSV (7200 mL.g⁻¹. h⁻¹), Feed ratio (H₂: CO₂: N₂ = 3:1:1).

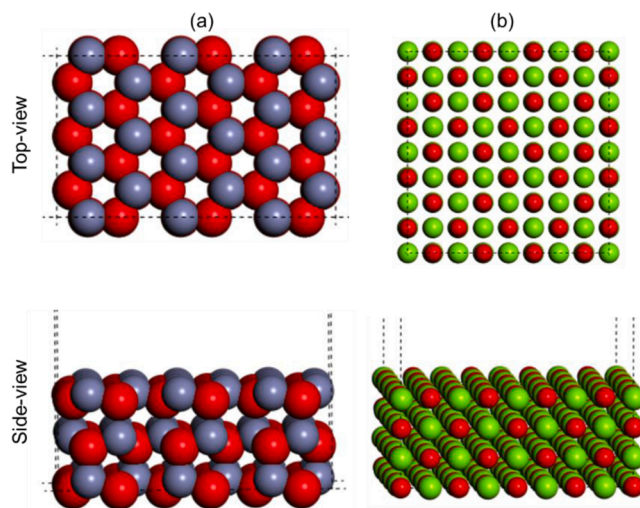


Fig. 12. The DFT optimized geometry of the active catalyst surfaces; (a) MgO(100); (b) ZnO(100). Color code: Zn (grey), O (red), Mg (green).

a small Mg₆O₇ cluster at the Cu₁₃-ZnO(100) surface at the Cu-ZnO interface, as shown in Fig. 13(c). The Cu₁₃/MgO/ZnO(100) surface model (Fig. 13(c)) represents the interface between the Cu particle and MgO/ZnO support. To represent the large Cu cluster, a Cu-strip/ZnO(100) model was created by adsorbing a two-layer of Cu-strip over the ZnO(100) surface, as shown in Fig. 13(d). The Cu-strip retains its overall geometry even after the adsorption at the ZnO(100) surface, as shown in Fig. 13(d).

Adsorption of CO₂ is studied over all the catalytically active model surfaces described above using the DFT method. The ZnO(100) surface was found to be not active for the CO₂ activation as the CO₂ does not get adsorbed at the ZnO(100) surface, as shown in Fig. 14(a). The CO₂ only gets physically adsorbed at a distance of 3.6 Å from the surface. Whereas the MgO(100) surface actively binds the CO₂ molecule forming a strong Mg-O(CO) bond (2.81 Å), as can be seen in Fig. 14(b). The adsorption energy of the CO₂ molecule to the MgO(100) surface was calculated to be -0.38 eV.

The interface of the Cu₁₃/ZnO(100) catalyst surface was found to be active for CO₂ activation, as can be seen from the CO₂ adsorption geometry in Fig. 15(a). The CO₂ molecule adsorbs strongly at the Cu₁₃ and ZnO(100) interface, forming bonds to the ZnO surface and Cu₁₃ nanocluster. The Zn-O, Cu-C, and Cu-O bonds were measured to be 2.04 Å, 2.05 Å, and 2.05 Å, respectively. The adsorption energy of CO₂ at the Cu₁₃/ZnO(100) catalyst surface was calculated to be -0.69 eV. Similar to the Cu₁₃/ZnO(100) catalyst surface, the Cu₁₃/MgO(100) catalyst surface also activates the CO₂ by adsorbing at the Cu₁₃/MgO interface, as shown in Fig. 15(b). The CO₂ molecule forms bonds to both the MgO(100) surface and the Cu₁₃ nanocluster. The Mg-O, Cu-C, and Cu-O bonds were measured to be 2.12 Å, 2.05 Å, and 2.08 Å, respectively. The adsorption energy of CO₂ at the Cu₁₃/MgO(100) catalyst surface was calculated to be -1.25 eV, which is 0.56 eV stronger compared to the Cu₁₃/ZnO(100) surface. The stronger adsorption energy at the Cu-MgO interface compared to the Cu-ZnO interface will enhance the CO₂ adsorption, as shown in the CO₂ chemisorption experiment. The basic nature of the MgO support can be the probable reason for the higher CO₂ adsorption at the Cu-MgO interface compared to the Cu-ZnO interface. To understand the promoting effect of MgO on the CO₂ adsorption Cu₁₃/MgO/ZnO(100) surface model is studied as shown in Fig. 15(c). The addition of the Mg₆O₇ cluster at the Cu₁₃/ZnO interface drastically enhance the CO₂ binding from -0.69 eV in Cu₁₃/ZnO(100) to -1.04 eV in Cu₁₃/MgO/ZnO(100), indicating the promotional effect of MgO in the CO₂ conversion over conventional Cu/ZnO catalysts, as also observed experimentally. At the Cu₁₃/MgO/ZnO(100) surface, the CO₂ binds to the Cu/MgO interface forming Mg-O (2.11 Å) and Cu-C (2.05 Å) bonds,

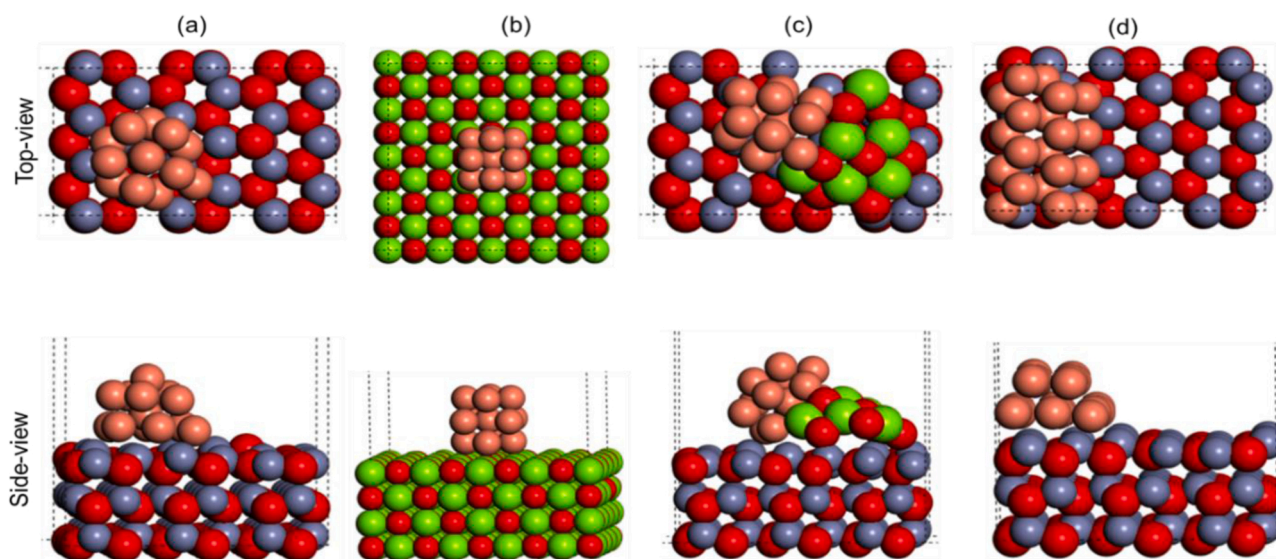


Fig. 13. The DFT optimized geometry of the active catalyst surfaces, (a) $\text{Cu}_{13}\text{-MgO}(100)$; (b) $\text{Cu}_{13}\text{-ZnO}(100)$; (c) $\text{Cu}_{13}\text{-MgO-ZnO}(100)$ and (d) $\text{Cu-strip-ZnO}(100)$. Color code: Zn (grey), O (red), Mg (green), Cu (orange), C (black).

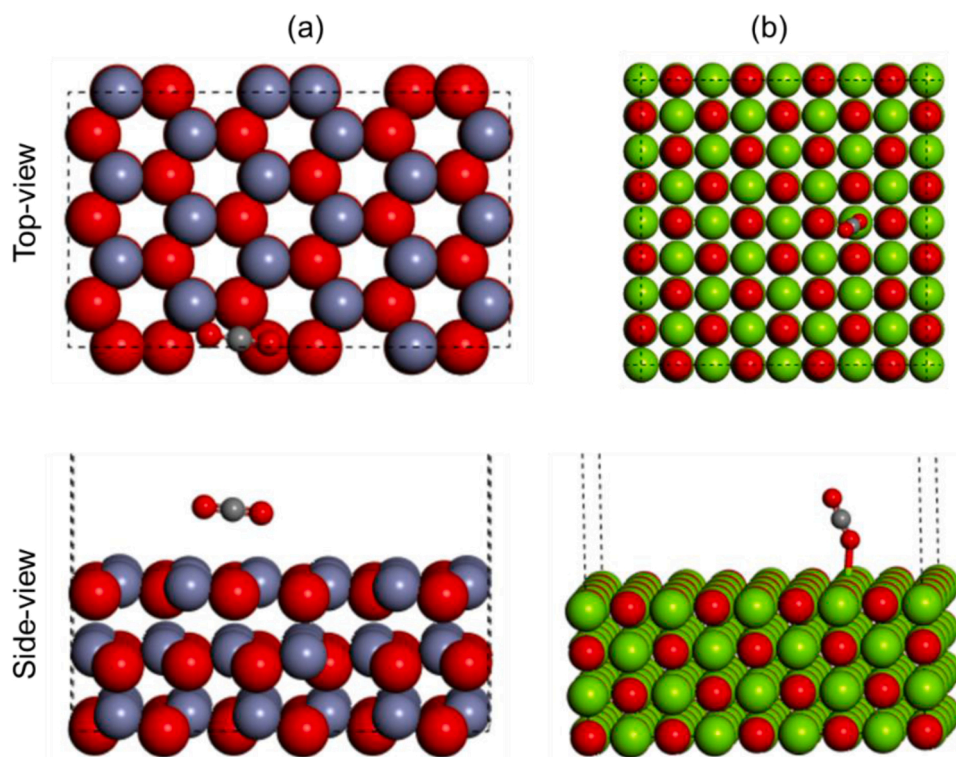


Fig. 14. The DFT optimized geometry of the CO_2 adsorption at the active catalyst surfaces; (a) $\text{MgO}(100)$ and (b) $\text{ZnO}(100)$. Color code: Zn (grey), O (red), Mg (green), Cu (orange), C (black).

as shown in Fig. 15(c). CO_2 adsorption study at the Cu-strip/ $\text{ZnO}(100)$ catalyst surface, representing the larger Cu particles at the ZnO support, show no chemical adsorption of CO_2 (Cu-C bond distance ~ 3.78 Å), as shown in Fig. 15(d), indicating the low activity of the larger Cu particles compared to the small metal cluster. This is also in accordance with the experimental findings where catalysts with high dispersion and small particle size showed higher CO_2 to methanol conversion.

5. Conclusion

MgO promoted Cu/ ZnO catalysts prepared by hydrothermal method using cetyltrimethylammonium bromide as morphology controlling agent and poly (diallyldimethylammonium chloride) as a structure-directing agent produce small Cu particles with high Cu surface area, and dispersion, which directly influence the catalytic performances. The addition of basic MgO decreased the surface density of Cu during synthesis, which increases the dispersion of Cu species and also favours the adsorption of CO_2 and 20 % MgO loading showed superior catalytic

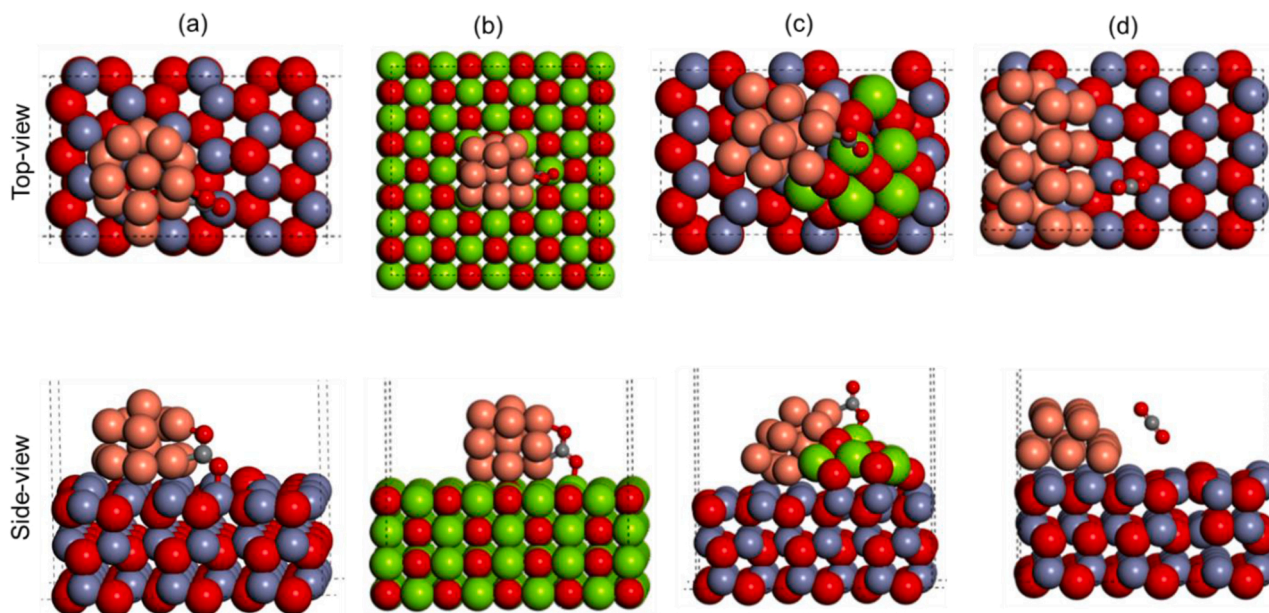


Fig. 15. The DFT optimized geometry of the CO_2 adsorption at the active catalyst surfaces; (a) $\text{Cu}_{13}/\text{ZnO}(100)$; (b) $\text{Cu}_{13}/\text{MgO}(100)$; (c) $\text{Cu}_{13}/\text{MgO}/\text{ZnO}(100)$ and (d) $\text{Cu-strip}/\text{ZnO}(100)$. Color code: Zn (grey), O (red), Mg (green), Cu (orange), C (black).

activity, high stability, and $> 99\%$ selectivity. XRD confirms that the addition of MgO decreases the lattice parameters of ZnO, where some Zn atom is replaced by Mg atom in the ZnO lattice, which favours the formation of reactive intermediates. H_2 -TPR also shows that the metal support interaction is present for 20 wt% MgO promoted Cu/ZnO ($\text{CMZ-20}^{\text{HT}}$) catalyst, which favours the stability of active Cu particles against sintering. The average Cu particle size was < 5 nm, and the presence of highly disperse surface-active Cu sites led to maximum CO_2 conversion of 8.7 % at 200°C with $> 99\%$ methanol selectivity, and the catalyst showed the methanol production rate of $0.0063 \text{ mol g}_{\text{Cu}}^{-1} \text{ h}^{-1}$. With increasing temperature, CO_2 conversion reached to 16.0 % at 300°C with 62 % methanol selectivity. $\text{CMZ-20}^{\text{HT}}$ catalyst is highly stable during CO_2 hydrogenation, and the catalyst did not show any deactivation even after 120 h time-on-stream. DFT calculation showed that the adsorption energy of CO_2 at the $\text{Cu}_{13}/\text{MgO}/\text{ZnO}(100)$ catalyst surface was calculated to be -1.04 eV , which is 0.35 eV stronger compared to the $\text{Cu}_{13}/\text{ZnO}(100)$ surface. The stronger adsorption energy at the Cu/MgO/ZnO interface compared to the Cu-ZnO interface will enhance the CO_2 adsorption, which in turn increases the CO_2 conversion over the Cu/MgO/ZnO catalyst. The activity and high methanol selectivity of the $\text{CMZ-20}^{\text{HT}}$ catalyst is the combination of the presence of large Cu surface area, very small Cu particles with high Cu dispersion, and the synergistic interaction between small Cu particles and ZnO support in the presence of MgO.

CRediT authorship contribution statement

Sachin Kumar Sharma: Design and performing experiment of the research work, manuscript writing and correction. **Tuhin Suvra Khan:** Design and performing DFT studies, manuscript writing and correction. **Rajib Kumar Singha:** manuscript writing and correction. **Bappi Paul:** manuscript writing and correction. **Mukesh Kumar Poddar:** catalyst characterization, manuscript writing and correction. **Takehiko Sasaki:** catalyst characterization, manuscript writing and correction. **Ankur Bordoloi:** Manuscript writing and correction. **Chanchal Samanta:** Manuscript writing and correction. **Shelaka Gupta:** Design DFT studies, manuscript writing and correction. **Rajaram Bal:** Conceptualization and Design the whole study, design of experiment of the research work, manuscript writing and correction.

Declaration of Competing Interest

The authors declare that they have no known competing financial interests or personal relationships that could have appeared to influence the work reported in this paper.

Acknowledgments

SKS acknowledges the Petrotech Society of India for providing research fellowship. CS and RB acknowledge Petrotech Society of India for providing support for a collaborative research project between Bharat Petroleum Corporation Ltd. (BPCL) and CSIR-IIP, Dehradun. CS acknowledges higher management of BPCL, Corporate research, and development center for granting permission to carry out this collaborative research work. B.P acknowledges SERB-DS-T for research funding (R/JF/2020/000042). The XAFS measurements were performed at KEK-IMSS-PF with the approval of the Photon Factory Advisory Committee (project 2017G190). The Director, CSIR-IIP, is acknowledged for his help and encouragement. The authors thank the Analytical Science Division, Indian Institute of Petroleum, for analytical services.

Appendix A. Supplementary data

Supplementary material related to this article can be found, in the online version, at doi:<https://doi.org/10.1016/j.apcata.2021.118239>.

References

- [1] P. Gao, S. Li, X. Bu, S. Dang, Z. Liu, H. Wang, L. Zhong, M. Qiu, C. Yang, J. Cai, *Nat. Chem.* 9 (2017) 1019–1024.
- [2] B.M. Tackett, E. Gomez, J.G. Chen, *Nat. Catal.* 2 (2019) 381–386.
- [3] O. Martin, A.J. Martin, C. Mondelli, S. Mitchell, T.F. Segawa, R. Hauert, C. Drouilly, D. Curulla-Ferré, J. Pérez-Ramírez, *Angew. Chem. Int. Ed.* 55 (2016) 6261–6265.
- [4] G. Bonura, M. Cordaro, C. Cannilla, F. Arena, F. Frusteri, *Appl. Catal. B: Environ.* 152 (2014) 152–161.
- [5] H. Ban, C. Li, K. Asami, K. Fujimoto, *Catal. Commun.* 54 (2014) 50–54.
- [6] X. Guo, D. Mao, G. Lu, S. Wang, G. Wu, *J. Catal.* 271 (2010) 178–185.
- [7] B. Hu, Y. Yin, G. Liu, S. Chen, X. Hong, S.C.E. Tsang, *J. Catal.* 359 (2018) 17–26.
- [8] R. Ladera, F.J. Pérez-Alonso, J.M. González-Carballo, M. Ojeda, S. Rojas, J.L. F. Fierro, *Appl. Catal. B: Environ.* 142 (2013) 241–248.
- [9] F. Arena, G. Mezzatesta, G. Zafarana, G. Trunfio, F. Frusteri, L. Spadaro, *J. Catal.* 300 (2013) 141–151.

- [10] J. Wang, G. Li, Z. Li, C. Tang, Z. Feng, H. An, H. Liu, T. Liu, C. Li, *Sci. Adv.* 3 (2017), e1701290.
- [11] C.H. Bartholomew, *Appl. Catal. A* 212 (2001) 17–60.
- [12] M.V. Twigg, M.S. Spencer, *Top. Catal.* 22 (2003) 191–203.
- [13] H. Lei, R. Nie, G. Wu, Z. Hou, *Fuel* 154 (2015) 161–166.
- [14] C. Tisseraud, C. Comminges, T. Belin, H. Ahouari, A. Soualah, Y. Pouilloux, A. Le Valant, *J. Catal.* 330 (2015) 533–544.
- [15] W.-C. Liu, J. Baek, G.A. Somorjai, *Top. Catal.* 61 (2018) 530–541.
- [16] I. Ganesh, *Renewable Sustainable Energy Rev.* 31 (2014) 221–257.
- [17] M. Pérez-Fortes, J.C. Schöneberger, A. Boulamanti, E. Tzimas, *Appl. Energy* 161 (2016) 718–732.
- [18] F. Liao, Y. Huang, J. Ge, W. Zheng, K. Tedsree, P. Collier, X. Hong, S.C. Tsang, *Angew. Chem. Int. Ed.* 50 (2011) 2162–2165.
- [19] C. Li, X. Yuan, K. Fujimoto, *Appl. Catal. A* 469 (2014) 306–311.
- [20] M.D. Porosoff, B. Yan, J.G. Chen, *Energy Environ. Sci.* 9 (2016) 62–73.
- [21] J. Nakamura, I. Nakamura, T. Uchijima, T. Watanabe, T. Fujitani, *Model studies of methanol synthesis on copper catalysts. Stud. Surf. Sci. Catal.*, Elsevier, 1996, pp. 1389–1399.
- [22] T. Fujitani, I. Nakamura, *Bull. Chem. Soc. J.* 75 (2002) 1393–1398.
- [23] J. Wu, M. Saito, M. Takeuchi, T. Watanabe, *Appl. Catal. A* 218 (2001) 235–240.
- [24] L. Wang, L. Yang, Y. Zhang, W. Ding, S. Chen, W. Fang, Y. Yang, *Fuel Process. Technol.* 91 (2010) 723–728.
- [25] M. Mureddu, I. Ferino, A. Musinu, A. Ardu, E. Rombi, M.G. Cutrufello, P. Deiana, M. Fantauzzi, C. Cannas, *J. Mater. Chem. A* 2 (2014) 19396–19406.
- [26] M. Mureddu, F. Ferrara, A. Pettinau, *Appl. Catal. B: Environ.* 258 (2019), 117941.
- [27] M. Huš, V.D. Dasireddy, N.S. Štefanič, B. Likozar, *Appl. Catal. B: Environ.* 207 (2017) 267–278.
- [28] X. Guo, D. Mao, G. Lu, S. Wang, G. Wu, *J. Mol. Catal. A: Chem.* 345 (2011) 60–68.
- [29] W. Zhang, H. Wang, W. Wei, Y. Sun, *J. Mol. Catal. A: Chem.* 231 (2005) 83–88.
- [30] L. Madeira, R. Martín-Aranda, F. Maldonado-Hódar, J. Fierro, M. Portela, *J. Catal.* 169 (1997) 469–479.
- [31] V.D. Dasireddy, S.S. Neja, L. Blaž, *J. CO₂ Util.* 28 (2018) 189–199.
- [32] L. Xu, H. Song, L. Chou, *Appl. Catal. B: Environ.* 108 (2011) 177–190.
- [33] R.K. Singha, A. Yadav, A. Agrawal, A. Shukla, S. Adak, T. Sasaki, R. Bal, *Appl. Catal. B: Environ.* 191 (2016) 165–178.
- [34] V. Tiwari, J. Jiang, V. Sethi, P. Biswas, *Appl. Catal. A* 345 (2008) 241–246.
- [35] H. Ren, C.-H. Xu, H.-Y. Zhao, Y.-X. Wang, J. Liu, J.-Y. Liu, *J. Ind. Eng. Chem.* 28 (2015) 261–267.
- [36] G. Delahay, D. Valade, A. Guzman-Vargas, B. Coq, *Appl. Catal. B: Environ.* 55 (2005) 149–155.
- [37] B.M. Abu-Zied, W. Schwieger, A. Unger, *Appl. Catal. B: Environ.* 84 (2008) 277–288.
- [38] A. Scarabello, D. Dalle Nogare, P. Canu, R. Lanza, *Appl. Catal. B: Environ.* 174 (2015) 308–322.
- [39] V.A. Kondratenko, C. Berger-Karin, E.V. Kondratenko, *ACS Catal.* 4 (2014) 3136–3144.
- [40] M. Rouchdi, E. Salmani, B. Fares, N. Hassanain, A. Mzerd, *Res. Phys.* 7 (2017) 620–627.
- [41] S. Li, Y. Xu, Y. Chen, W. Li, L. Lin, M. Li, Y. Deng, X. Wang, B. Ge, C. Yang, *Angew. Chem. Int. Ed.* 56 (2017) 10761–10765.
- [42] W. Li, G. Zhang, X. Jiang, Y. Liu, J. Zhu, F. Ding, Z. Liu, X. Guo, C. Song, *ACS Catal.* 9 (2019) 2739–2751.
- [43] G. Chinchén, K. Waugh, D. Whan, *Appl. Catal.* 25 (1986) 101–107.
- [44] W. Pan, R. Cao, D. Roberts, G. Griffin, *J. Catal.* 114 (1988) 440–446.
- [45] C. Baltes, S. Vukojević, F. Schüth, *J. Catal.* 258 (2008) 334–344.
- [46] S. Natesakhawat, J.W. Lekse, J.P. Baltrus, P.R. Ohodnicki Jr., B.H. Howard, X. Deng, C. Matranga, *ACS Catal.* 2 (2012) 1667–1676.
- [47] D. Uzio, G. Berhault, *Catal. Rev.* 52 (2010) 106–131.
- [48] R. Rioux, H. Song, J. Hoefelmeyer, P. Yang, G. Somorjai, *J. Phys. Chem. B* 109 (2005) 2192–2202.
- [49] M. Zabilskiy, P. Djinović, E. Tchernychova, O.P. Tkachenko, L.M. Kustov, A. Pintar, *ACS Catal.* 5 (2015) 5357–5365.
- [50] L. Pino, A. Vita, F. Cipiti, M. Laganà, V. Recupero, *Appl. Catal. B: Environ.* 104 (2011) 64–73.
- [51] R.K. Singha, A. Shukla, A. Yadav, S. Sain, C. Pendem, L.S.K. Konathala, R. Bal, *Mol. Catal.* 432 (2017) 131–143.
- [52] S. Kuld, C. Conradsen, P.G. Moses, I. Chorkendorff, J. Sehested, *Angew. Chem. Int. Ed.* 53 (2014) 5941–5945.
- [53] I. Melián-Cabrera, M.L. Granados, J. Fierro, *J. Catal.* 210 (2002) 273–284.
- [54] B. Sarkar, C. Pendem, L.S. Konathala, R. Tiwari, T. Sasaki, R. Bal, *Chem. Commun.* 50 (2014) 9707–9710.
- [55] N. Siddiqui, B. Sarkar, C. Pendem, L.S. Konathala, T. Sasaki, A. Bordoloi, R. Bal, *Catal. Sci. Technol.* 7 (2017) 2828–2837.
- [56] M.N. Barroso, M.F. Gomez, J.A. Gamboa, L.A. Arrúa, M.C. Abello, *J. Phys. Chem. Solids* 67 (2006) 1583–1589.
- [57] M.M.-J. Li, Z. Zeng, F. Liao, X. Hong, S.C.E. Tsang, *J. Catal.* 343 (2016) 157–167.
- [58] F. Liao, Y. Huang, J. Ge, W. Zheng, K. Tedsree, P. Collier, X. Hong, S.C. Tsang, *Angew. Chem.* 123 (2011) 2210–2213.
- [59] Y. Sun, C. Huang, L. Chen, Y. Zhang, M. Fu, J. Wu, D. Ye, *J. CO₂ Util.* 37 (2020) 55–64.
- [60] J.T. Sun, I.S. Metcalfe, M. Sahibzada, *Ind. Eng. Chem. Res.* 38 (1999) 3868–3872.
- [61] C. Liu, B. Yang, E. Tyo, S. Seifert, J. DeBartolo, B. von Issendorff, P. Zapol, S. Vajda, L.A. Curtiss, *J. Am. Chem. Soc.* 137 (2015) 8676–8679.
- [62] G.K. Ramesha, J.F. Brennecke, P.V. Kamat, *ACS Catal.* 4 (2014) 3249–3254.